Robust and effective automatic parameter choice for medical image filtering.

Ana João[+], Alberto Gambaruto[*], Ricardo Pereira[b], Adélia Sequeira[+]

[*] *Department of Mechanical Engineering*
University of Bristol
Queen's Building, University Walk, Bristol BS8 1TR, UK.

[b] *Department of Neurosurgery, Coimbra University Hospital Center*
Faculty of Medicine, University of Coimbra
Rua Larga, 3004-504 Coimbra, Portugal

[+] *Departamento de Matemática and CEMAT/IST*
Instituto Superior Técnico, Technical University of Lisbon
Av. Rovisco Pais 1, 1049-001 Lisboa, Portugal

Abstract

The analysis of medical image data currently requires the interpretation of a trained and experienced user. The technological advances in imaging machinery and the understanding of disease onset, as well as medical planning, all favour the need for ever more automatic and robust methods for evaluating the health state of a subject. Here, we concentrate on methods for processing medical image data, as currently provided by existing imaging technologies, in particular the effectiveness of automatic image filtering in order to remove noise and improve the sharpness of distinct objects. The filtering approach is based on a partial differential equation, namely the Perona-Malik anisotropic diffusion equation. The approach adopted for terminating the iterative filtering procedure is based on image quality descriptors. In specific, we observe the rate of change of these to infer the transient effects of the filtering process. The entire pipeline is demonstrated to work effectively on different sets of medical image data, including MRI, CTA and CT, both in individual 2-D images in a stack, as well as treating the complete 3D volumetric dataset.

Keywords:
Medical imaging processing, image quality, Perona-Malik filtering, automatic algorithm, object segmentation

1. Introduction

The importance of medical imaging has increased rapidly in the last decades, in the diagnosis and evaluation of a wide range of pathologies. Medical imaging acquisition systems inevitably introduce noise and are limited in resolution, reducing the apparent quality and ease of analysis of the data. Additionally, imaging artefacts may further deteriorate the image dataset and introduce unwanted features. In practice, medical image datasets can be thought to contain uncertainties that hinder a clear analysis or interpretation. The degradations may be attenuated to some extent by filtering algorithms in a post-processing step, and in doing so extend the scope and use of a given dataset. The filtering process, as all image processing, should not destroy meaningful anatomical detail nor erroneously create features, which could compromise an accurate interpretation of the medical image data. Image filtering is not only essential in medical imaging applications for noise removal, but also to enhance and recover fine details that may not otherwise be easily detected.

The research community has focused on the design of fast and robust methodologies to remove noise without distorting clinically relevant data [2, 3, 4, 10]. Image processing methods, beyond filtering, also serve to improve and facilitate an accurate interpretation of the medical image data, for example: contrast enhancement, bias correction, and shape detection [8, 9, 19, 22, 42]. The methods introduced above to improve image quality, support the advances in imaging equipment technology, complementing them but largely retaining their role as post-processing techniques.

An important step in medical image analysis and clinical evaluation is the delineation of relevant objects, hence object segmentation and extraction. The segmentation and reconstruction of a 3D virtual model is additionally a key component of mathematical modelling and numerical simulations of patient specific cases, in a range of topics. The computer simulation of human physiology has been influential in furthering our understanding of the mechanical and biological functioning, especially in relation to a number of diseases and pathologies. However, these simulations are sensitive to variations in the reconstructed 3D virtual model that naturally arise from the uncertainty present in medical images [11, 34]. It is of great interest therefore, to process medical images with emphasis on object segmentation, with an algorithm that performs both automatically, to ensure both repeatability of results, and accurately, to retain fidelity to the raw medical data.

Methods in image processing based on partial differential equations have been widely used due to their successful performance in reducing noise while preserving important features, such as object or region edges. Their scope is not limited to the image denoising problem, but also other restoration tools such as deblurring, enhancement, edge detection and segmentation. Here, we focus our work on the use of the anisotropic diffusion method, largely studied since its formulation by Perona and Malik [30], known commonly as the Perona-Malik (PM) equation. This model has benefited from much attention of the research community, is considered a simple and valuable tool for image filtering and is consequently still commonly used. However, this method is affected by the correct choice of parameters needed, namely the gradient threshold selected for the conductance function and the diffusion time (or number of iterations), which together form the set of parameters that define the behaviour and amount of diffusion. Incorrect estimation of the parameters may lead to an over-filtered, blurry image or an under-filtered one.

Several works have investigated both the theoretical and computational aspects of the Perona-Malik anisotropic diffusion model. Regarding the theoretical behaviour, the ill-posedness of the PM equation makes it difficult to derive analytical results estimating the behaviour [16, 17, 1], and some authors have therefore focused on developing new well-posed models or regularising methods, see [16, 17] and references therein. Computationally, filtering algorithms created from discretisations of the PM equation have shown limitations, such as poor performance in flat regions that result in the well known *staircasing* artefact. Beyond these concerns, the task of automatic choice of parameters for the PM equation has not been satisfactorily addressed.

Investigation of the appropriate stopping criteria to the filtering by anisotropic diffusion has seen some mixed success, and on the whole the works rely on synthetic images as opposed to real world images. In Gilboa et al. [13], it was shown that stopping in the steady state with respect to signal-to-noise ratio (SNR) yields an overly smooth image. In Dolcetta and Ferrati [7] the stopping criteria is defined as the minimum of the performance index. This index is found *a priori* using a synthetic image with similar details and discontinuities to the one to be filtered. Sporring and Weickert [33] proposed that the stropping criteria is based on the signal-to-noise ratio and the relative variance at each iteration, and the image information known at the beginning of the diffusion process. A comparison of the spectral content of the iterations with that of a smoothed image was usind in restoration of corrupted images [21] and medical image processing [25]. Other approaches have been introduced to choose a stopping criterion, largely making use of statistical data [43, 35] or spatial entropy [24, 23].

Equally important, the diffusion coefficient should be carefully chosen to ensure correct identification of the threshold between desired object and noise scales. It was suggested [26] that the diffusion coefficient should to be a decreasing function of time, consequently preserving edges above this decreasing threshold as the filtering progresses. Other methods for estimating this parameter have been proposed, for example using statistical characteristics of the initial image and morphological operators [5, 28, 36, 12].

In the present work, we set out to investigate the quality of the processed images in order to obtain an automatic filtering algorithm. The Perona-Malik anisotropic diffusion method is employed, and hence the parameters to be automatically chosen are both the gradient threshold (in the diffusion coefficient equation) and the diffusion time. Unlike previous studies, the parameter choice is found independently for each datasets and makes use of image quality metrics. No *a priori* information or estimated parameter is necessary, but may be used to speed up the computational time by restricting the permissible variable range. Additionally, we compare the anisotropic diffusion filter in two and three dimensions when applied to medical imaging datasets.

The paper is organised as follows. Details of the synthetic and medical data used are described in section 2. Section 3 includes a detailed description of the image quality metrics used to analyse an image and optimize the automatic selection of parameters. A brief introduction to the Perona-Malik model is provided in section 4. The proposed automatic selection of the stopping criteria and gradient threshold is detailed in section 5. Some preliminary but promising results are presented in section 6. Discussion and conclusions of the proposed automatic filtering methodology are finally given in section 7.

2. Test images and patient specific datasets

In this work, in order to obtain meaningful insight of the outputs produced by the automatic denoising algorithms in one, two and three dimensions, different datasets have been chosen. This provides us with a varied set of numerical tests in order to infer generality of the methodology.

Image type	Image ID	Dataset	Resolution
Synthetic	1	step functions	1/140
	2	$f(x) = sin(x) + cos(3x)$	0.2π
	3	binary circle with 10% Gaussian noise	100 pixels / diameter
Medical images	4	Cerebral aneurysm (CTA)	$(0.28 \times 0.28 \times 0.4)$ /mm
	5	Cerebral aneurysm (CTA)	$(0.26 \times 0.26 \times 0.6)$ /mm
	6	Cerebral aneurysm (CTA)	$(0.39 \times 0.39 \times 0.5)$ /mm
	7	Cerebral aneurysm (CTA)	$(0.265 \times 0.265 \times 0.8)$ /mm
	8	Nasal cavity (CT)	$(0.49 \times 0.49 \times 0.6)$ /mm
	9	Cerebral ventricular system (MRI)	$(0.48 \times 0.48 \times 1.45)$ /mm

Table 1: Image datasets used for numerical validation in the present work.

We denote an image as a 2-dimensional orthogonal domain $\Omega = (1, N_x) \times (1, N_y)$, with N_x and N_y being the height and width of the image respectively, measured as the number of row and columns. In 3-dimensions, a stack of 2-dimensional images is considered, hence $\Omega = (1, N_x) \times (1, N_y) \times (1, N_z)$, with N_z being the depth of the volume, measured as the number of slices in the stack. The greyscale pixel intensity of the dataset has been normalised to $[0 - 255]$. Let us denote the image during its processing by $I_t = I(x, y, t)$, where x, y are the integer valued coordinates of a pixel in the image, and t denotes the integration time (or the integer valued time step count) of the diffusion process. The original 2-dimensional image is hence denoted by $I_0 = I(x, y, 0)$.

Several tests are performed numerically in order to evaluate if the proposed methodology is robust and effective in image filtering. The datasets comprise of both synthetic images and patient-specific medical image scans, shown in (Figures 1 and 2), and summarised in Table 1. The tests involve employing the filtering method to 1D, 2D and 3D signals, to incrementally evaluate the filtering action and the importance of the parameter choice in the anisotropic diffusion method.

3. Image quality measures

The effects of the image processing may be assessed by quantifying the image quality, including an estimate for the amount of noise present. This is relevant not only when analysing the accuracy of both denoising or object extraction algorithms, but also in order to adapt any algorithm parameter that may be dependent on the image characteristics. In this work we are interested in tuning the filtering process based on the following factors: *i) reduction of noise; ii) image quality based on comparison; iii) object edge preservation*.

We analyse the local variance of the image intensity as a measure of image noise, since for a binary image high values of variance are seen only at feature edges. At a given pixel $I(i, j)$, the local (biased) variance σ^2, in a surrounding region of interest of size $n \times n$, is given by

$$\sigma^2(I(i, j)) = \frac{1}{n^2} \sum_{X=-\frac{n-1}{2}}^{\frac{n-1}{2}} \sum_{Y=-\frac{n-1}{2}}^{\frac{n-1}{2}} \Big(I(i + X, j + Y) - \mu \Big)^2 \tag{1}$$

where μ is the mean intensity of the local region of interest, and n is a positive, odd-valued integer. In this work $n = 3$ was chosen, being the smallest symmetric mask size.

There are several measures of image quality, typically used to compare images. In the present study the unprocessed image is compared to those filtered at increasing stages. The quality metrics used are:

- *mean squared error*, $MSE = \frac{1}{n^2} \sum_{i=1}^{n} \sum_{j=1}^{n} [I_0(i, j) - I_t(i, j)]^2$.
- *peak-signal-to-noise-ratio*, $PSNR = 20 \log \left(\frac{256}{\sqrt{MSE}} \right)$
- *signal-to-mean-square-error*, $S/MSE = 10 \log \left(\frac{\sum_{i=1}^{n} \sum_{j=1}^{n} I_0(i,j)^2}{\sum_{i=1}^{n} \sum_{j=1}^{n} [I_0(i,j) - I_t(i,j)]^2} \right)$
- *contrast-to-noise-ratio*, CNR $= \frac{|r_A - r_B|}{\sigma}$, where r_A and r_B are respectively signal intensities for the region of interest and noise, and σ is the standard deviation of the image noise.

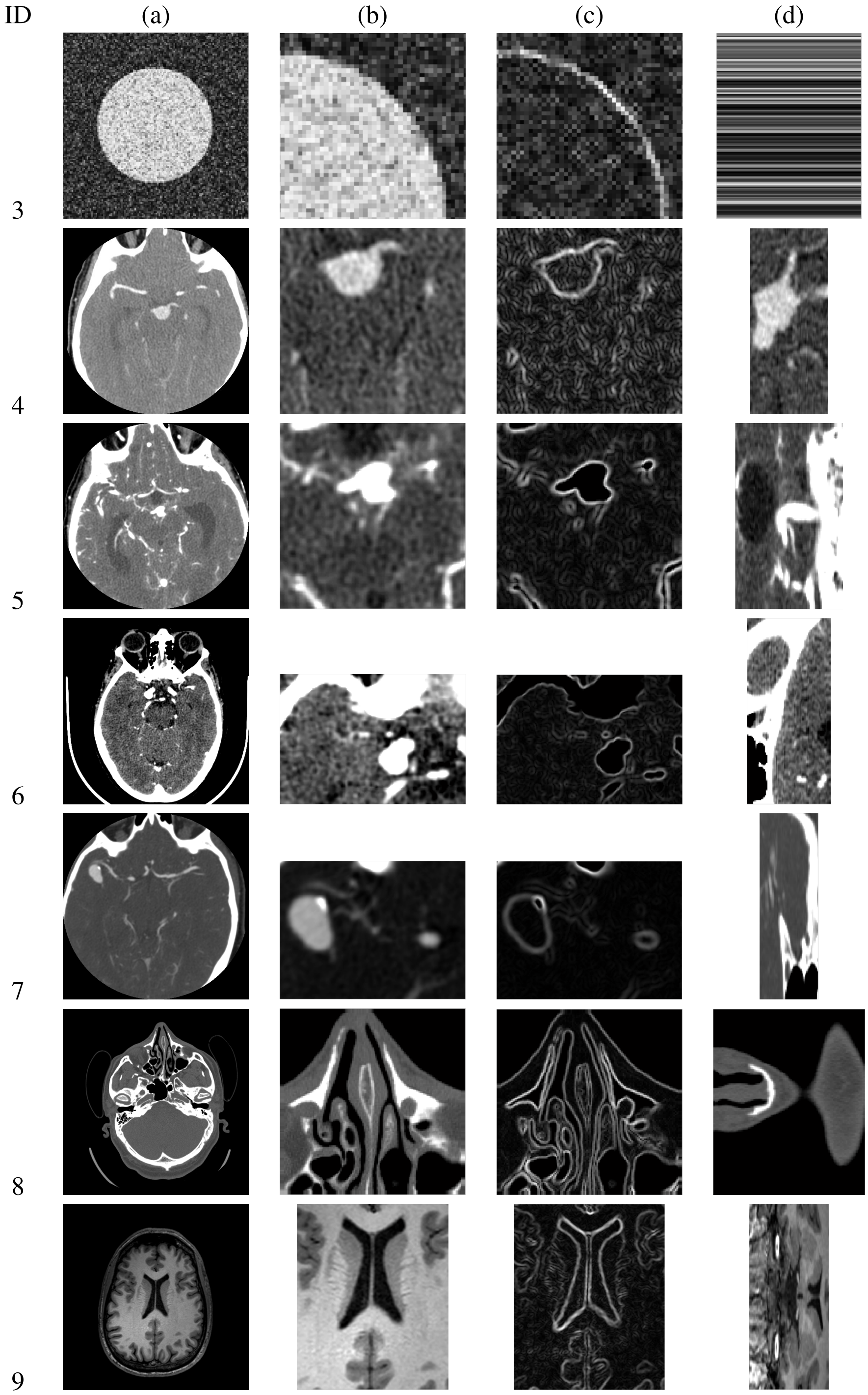

Figure 1: The medical image datasets are a stack of images acquired in the axial plane. For each, a representative image is considered: (a) original image showing the full acquisition dimensions; (b) the region of interest; (c) the image gradient for the region of interest; (d) section of the region of interest in the sagittal plane, highlighting the presence of inter-slice noise.

These measures are appealing due to their simplicity and clear physical meaning, however they lack visual quality perception. To complement these, the *structural similarity measure* (SSIM) is also considered [37], for which the original and filtered images are compared. The SSIM metric is based on the hypothesis that the human visual system is adapted for extracting structural information, and compares local patterns of pixel intensities normalised for luminance, contrast and structure.

The use of a set of image quality metrics will improve the analysis regarding the effectiveness of the filtering. The metrics are also used to guide the choice of optimal parameters in the anisotropic filtering equations.

Beyond image quality metrics, we are interested in preserving object edge location and improve edge definition. This is evaluated in the present work by object segmentation as a post-processing step. Segmentation is performed both on single image slices from of the dataset, as well as directly extracting a surface from the volumetric dataset. Object segmentation is performed based on the zero-crossing of the second directional derivatives of the image intensity [18, 27]. The approach adopted for computing the directional derivatives follows that proposed in [10], which allows for the removal of outliers on computing the derivatives.

4. Diffusion in Image Filtering

The general non-linear anisotropic (non-homogeneous) diffusion process looks for the solution of:

$$\begin{cases} \frac{\partial I}{\partial t} = \nabla \cdot (c\,\nabla I), & \text{in } \Omega \\ \\ I(0) = I_0 \end{cases} \tag{2}$$

where, $\Omega = \mathbb{R}^n$,$\nabla\cdot$ and ∇ represent the divergence and gradient operators respectively, and $c(x, y, z, t)$ is the diffusion coefficient, allowing for spatial anisotropy. Depending on the model chosen, c can be a scalar or a tensor/function, to allow for directional anisotropy [38, 41]. When c is chosen to be a function of the image I, (Eq. 2) becomes non-linear.

It is easily seen that if c is set to be a constant scalar, then Eq. 2 reduces to the isotropic heat equation. Solving the heat equation can be carried out by convolving the initial temperature distribution (i.e. image intensity) with a Gaussian kernel, which variance depends linearly on the total time of diffusion. The Gaussian function in fact is the Green's function (i.e. the impulse response) for the diffusion equation. This operation is commonly used in image filtering by radial weighted pixel intensity averaging within a given compact support.

4.1. An overview of the Perona-Malik method

The anisotropic diffusion method, also known as Perona-Malik (PM) model [30], makes use of a spatially varying diffusivity coefficient, such that smoothing occurs *within* regions rather than *across* region boundaries. Boundaries are commonly described as functions of $|\nabla I|$, though alternatively higher order derivatives may also be used [17].

The motivation for a spatially varying gradient threshold is the following. For small spatial gradients of the image pixel intensity, which can be considered as *homogeneous regions*, large values of the diffusivity are desirable in order to perform a stronger local smoothing, hence confidently removing the local noise. Conversely, in regions with large gradients, which can be considered as containing *region boundary*, smaller values of diffusivity are sought to reduce the diffusion process and preserve important image features. The diffusion coefficient c is, therefore, suggested to be a decreasing function of the spatial gradient and is commonly formulated based on two possibilities [30]. Both definitions are non-linear and space-invariant transformation of the initial image. In the present study, c in (Eq. 2) is given by

$$c = \frac{1}{1 + \left(\frac{|\nabla I|}{\beta}\right)^2} \tag{3}$$

By choosing this formulation, emphasis is given to wide regions over smaller ones [39]. It is shown in Appendix A that (Eq. 2) allows for backward diffusion in the direction normal to the ridges of I for large enough gradients $|\nabla I|$, while always maintaining a forward nature in ridge tangential directions.

Filtering discrete signals requires a reformulation of Eq. 2 for discrete computations. In the discrete case therefore, the local image gradients are computed as differences between neighbouring pixel intensities. For example, in the 1D case the spatial discretisation can be derived as follows:

$$
\begin{aligned}
\frac{\partial I}{\partial t} &= \nabla \cdot (c \nabla I) \\
&= \frac{\partial}{\partial x}\left(c \cdot \frac{\partial I(x,t)}{\partial x}\right) \\
&\simeq \frac{\partial}{\partial x}\left(c \cdot \frac{1}{\Delta x}\left(I(x+\frac{\Delta x}{2},t) - I(x-\frac{\Delta x}{2},t)\right)\right) \\
&\simeq \frac{1}{\Delta x^2}\left(\left[c(x+\frac{\Delta x}{2},t)\cdot(I(x+\Delta x)-I(x))\right] - \left[c(x-\frac{\Delta x}{2},t)\cdot(I(x-\Delta x)-I(x))\right]\right) \\
&= \phi_{east} - \phi_{west} \qquad \text{for} \quad \Delta x = 1
\end{aligned}
\tag{4}
$$

and finally adopting a first order time discretisation, we obtain

$$
I(t+\Delta t) \simeq I(t) + \Delta t \cdot \frac{\partial I}{\partial t} = I(t) + \Delta t \cdot (\phi_{east} - \phi_{west}) \tag{5}
$$

Stability of this one-dimensional scheme is achieved by appropriate choice of the time discretisation, such that $\Delta t < 1/2$ [40]. The two-dimensional discretisation of the procedure is presented in Appendix B. This scheme has been adopted due to its simplicity, though it should be noted that alternative and more computationally efficient approaches have been developed, based on operator splitting or factored schemes [15, 40, 32]

The behaviour of the anisotropic diffusion equation can be observed with simple tests. Here we take as examples two 1D functions: i) a smooth trigonometric function $f(x) = \sin(x) + \cos(3x)$, and ii) a series of incremental step functions. Additionally, on stacking these 1D function, one obtains a 2D image, which can in turn be stacked to obtain a 3D volume. For these datasets the image intensity varies only in one Cartesian direction, allowing for a simple analysis of the anisotropic filtering in different dimensions for effectively equivalent initial data. By considering these additional dimensions, the noise present will be interpreted according the dimension, and the filtering will additionally be performed in each Cartesian direction. Results of the anisotropic diffusion carried out in 1D, 2D and 3D are shown in Figure 2. We will see subsequently that the two-dimensional and three-dimensional experiments on the medical image datasets corroborate the one-dimensional findings. A significant difference is seen in terms of computational speed, while the same behaviour is seen for both the smooth trigonometric function and the step functions.

4.2. Overview of parameter choice for the Perona-Malik method

Filtering methods are sensitive to the choice and fine tuning of different parameters. The Perona-Malik method is mainly affected by the threshold β, which appears in the anisotropic diffusion coefficient (see Eq. 3), and the stopping criteria T, which is the total diffusion time ($T = \sum \Delta t$, see Eq. 5). Thus, a critical question is how to choose these two parameters for a given image dataset in order to obtain the most favourable filtering result.

The gradient threshold β plays a major role in the diffusion process, since it defines the difference between noise and object edges. Different approaches to estimate β have been proposed in the literature. Perona and Malik [30] suggested to fix β by trial and error, or using a *noise estimator* as described in [6]. Alternative approaches have been proposed, such as using the *p-norm* of the image intensity [36], or through linking robust local statistics estimators and diffusion [20, 5].

Let us now consider some of the different approaches found in the literature for selecting a stopping criteria. The main challenge when deciding an optimal stopping criteria lies in the fact that a noise free image is not always known a priori. Therefore, T should be estimated using only statistics of the filtered image at each iteration of the diffusion process. A decorrelation criteria was proposed in [29], in which T is considered as the time which minimizes the correlation between the difference $(I_0 - I_t)$ and I_t, where I_0 and I_t are the original image and filtered image after t iterations, respectively. Therefore,

$$
T = \arg\min_t \frac{\mathrm{cov}(I_0 - I_t, I_t)}{\sqrt{\mathrm{var}(I_0 - I_t)\cdot \mathrm{var}(I_t)}} \tag{6}
$$

Another approach suggested in [12] is to maximize the signal-to-noise-ratio (SNR) of the filtered image as:

$$
\mathrm{SNR} = 10 \log \frac{\mathrm{var}(I_c)}{\mathrm{var}(I_t - I_c)}. \tag{7}
$$

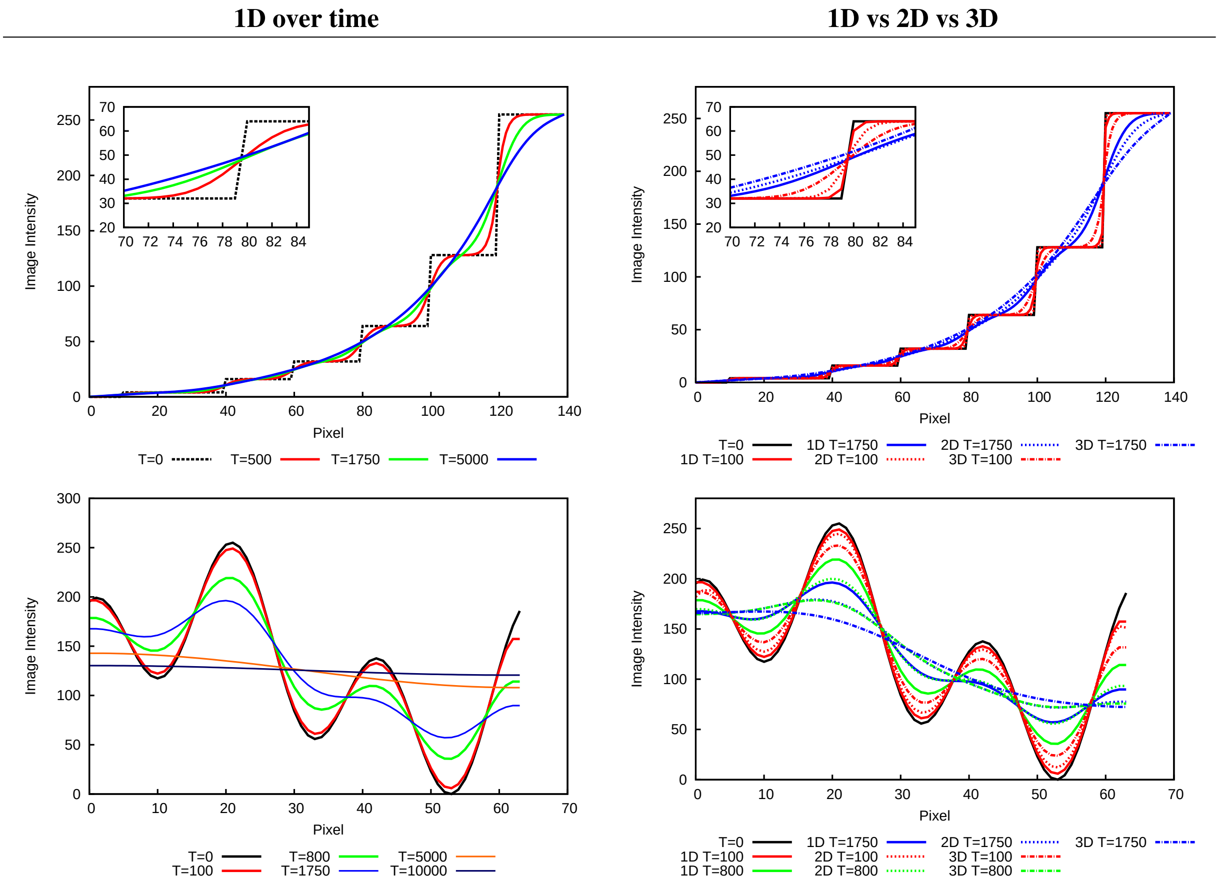

Figure 2: Typical evolution of the anisotropic diffusion method as proposed by the Perona-Malik method (Eqs. 2 and 3). Here $\beta = 1$, while the total integration time T is varied. Two test functions are considered: top row shows a sequence of incremental step functions; bottom row shows smooth trigonometric function. Left column: 1D filtering at different T. Right column: comparison between 1D, 2D and 3D filtering at different T.

where I_c is the noise free image, such that $I_0 = I_c + noise$. Given that $\partial(SNR)/\partial(\mathrm{var}(I_0 - I_t)) = 0$ yields the condition for finding the maximum of SNR, then T can be found as

$$T = \arg\min_t \frac{\partial_t \mathrm{cov}((I_0 - I_c), (I_0 - I_t))}{\partial_t \mathrm{var}(I_0 - I_t)}. \tag{8}$$

The variance of noise $(I_0 - I_c)$, however, has to be known a priori, and while this may be estimated it may lead to significant errors in practical applications.

A similar approach, proposed by [31], involves selecting T that maximizes the signal-to-mean-square-error S/MSE improvement, which is computed as the difference in S/MSE values at two consecutive time steps. Again, this is a very successful metric when dealing with synthetic images, where a noise free image is known beforehand.

All the above methods give emphasis to reducing noise and do not take into consideration the quality of object edges within the image. It has been shown in the literature that, over filtering the image (selection of T larger than the one needed) blurs feature edges and effectively degrades the image. It is clear that as an edge degrades the PSNR of the filtered image starts decreasing as well.

5. Automatic choice of gradient threshold β, and total integration time T

In the present work, both T and β are selected based on a combination of different metrics (defined earlier in Section 3): mean image variance (σ), mean square error (MSE), contrast-to-noise-ratio (CNR), structural similarity measure (SSIM), peak-signal-to-noise-ratio (PSNR). In doing so, both the overall image quality and the object edges are taken into consideration. While the aim is to identify preferred choice for parameters β and T in the filtering process, the concept of 'optimal' should be used loosely since no formal optimisation is performed.

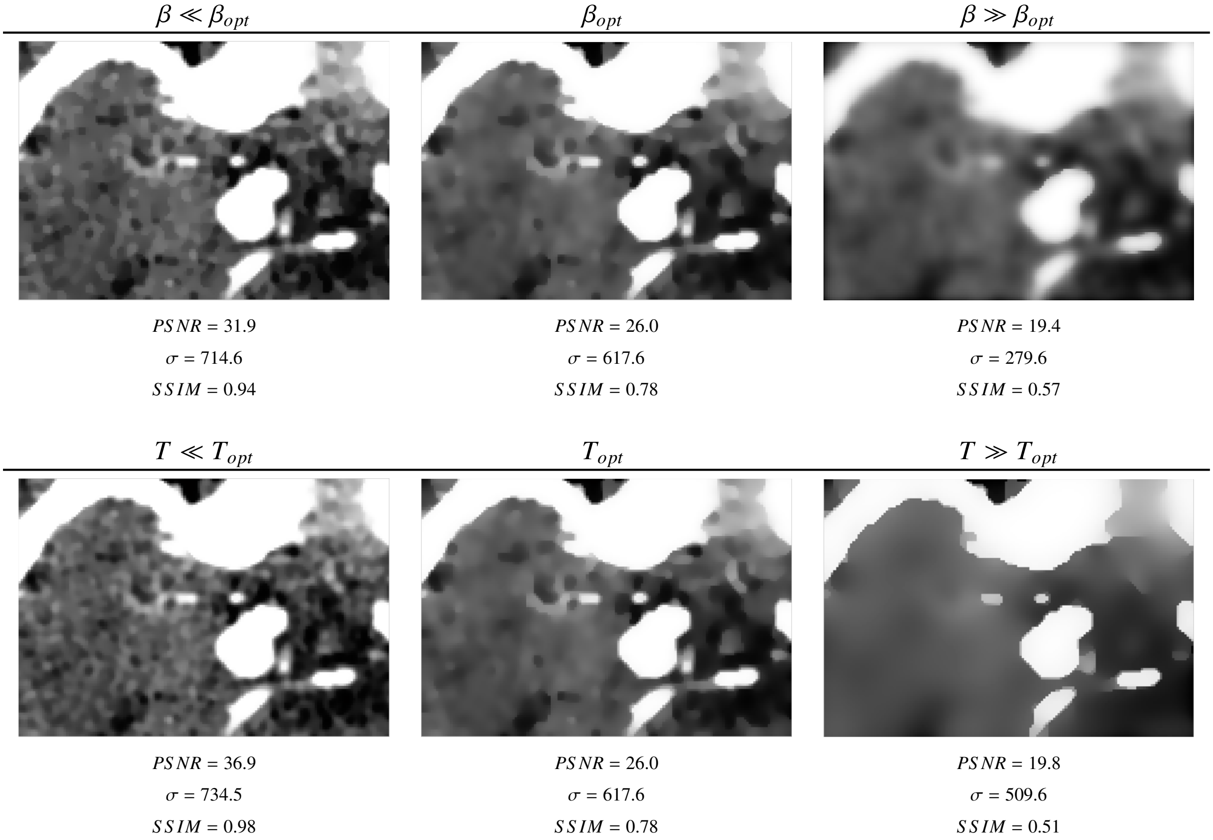

Figure 3: Image dataset 6, highlighting effects of under- and over-filtering based on alternative choices of β and T around the identified optimal values. Top row: varying the gradient threshold β, while $T = T_{opt}$. Bottom row: varying total integration time T, while $\beta = \beta_{opt}$.

However an exhaustive search is carried out, computing the image quality metrics for a range of parameters T and β, and subsequently identifying the most desirable image, as well as an acceptable parameter ranges. The effects of alternative choices of the parameters β and T around the identified optimal value are shown in Figure 3, from which under- and over-filtering can be visually appreciated.

The exhaustive parameter search proposed is a two stage process to reduce the computational cost. In the first stage, a range of β values are investigated. For each choice of β, the anisotropic diffusion is carried out and an optimal total integration time T is identified, based on image quality metrics, hence we write $T = T(\beta)$. The output of the first stage therefore, is a set of plausible filtered images, each computed with a different, incremental β and up to its optimal T. The second stage involves making use of image quality metrics on this set of filtered images, identifying the most desirable one. By doing so, the difficulty in identifying optimal choice for β and T is decoupled. Hence, an effective choice of T for a range of β is first computed, and subsequently the selection of the optimal β.

In both stages, one parameter is varied incrementally, which allows one to follow the filtering behaviour. In the first stage, for each choice of β, the diffusion integration time is advanced uniformly, while in the second stage the set of plausible filtered images are ordered by incremental β. The filtering behaviour is quantified by computing the rates of change of some image quality metrics, with respect to either T (in the first stage) or β (in the second stage). From these rates of change in image quality metrics, it is possible to identify different responses to the anisotropic diffusion as it progresses.

These rates of change are effectively the gradient ($\partial |f|/\partial t$), and Laplacian ($\partial^2 |f|/\partial t^2$), where f is replaced by each of the image quality metrics. For a constant time integration step Δt, the rates of change are based on the iteration count, which for simplicity can be considered of unit size. We can therefore write the discrete gradient as

$$\nabla f = f_{t+1} - f_t \tag{9}$$

and the discrete Laplacian as

$$\Delta f = \nabla f_{t+1} - \nabla f_t \tag{10}$$

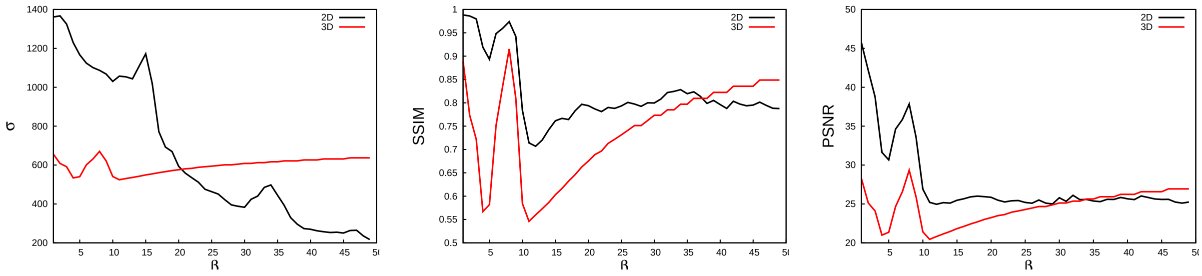

Figure 4: Example behaviour for image dataset 6, highlighting the use of quality metrics to optimize β and T. The filtering responds differently if an individual 2D image or volumetric 3D datasets are used. Note that $\beta_{opt} = 9; T(\beta = 9) = 55$.

where the subscript t is the time integration iteration count. The gradient of a image quality metric describes the progression of the image processing, while the Laplacian can be used as an indicator of changing regimes in the filtering process. In practice the ratio of Laplacian to gradient is employed as a single indicator function to present the progressive effects of the filtering procedure, hence:

$$F = \frac{|\Delta f|}{|\nabla f|} \tag{11}$$

The premise considered in a filtering process of an image corrupted by noise, is that it will contain information of the noise at a smaller scale to that of the foreground objects in the image. As the filtering progresses, the suppression of noise occurs faster than the deterioration of the image object definitions because the noise appears at the smaller scale. By observing the rate of change of the image quality metrics, the different stages of the filtering process are identifiable. Hence, we look to terminate the filtering when the removal of the noise has slowed down sufficiently, and before the foreground object definition starts degrading excessively. Consequently, we seek the instant in the filtering process where only small changes occur between two successive images, hence a small gradient. Additionally we look for the iteration step t where the Laplacian changes sign, since we seek a distinct change in the filtering process, namely when the noise (small scale features) are effectively removed and the image object boundaries become evidently affected.

In the first stage, for a given choice of β, the optimal number of iterations in the filtering process, hence the total integration time T of Equation 2, can be identified by observing the rates of change of the following image quality measures: the mean local image variance (σ), the contrast-to-noise ratio (CNR) and the structural similarity measure (SSIM), as a function of the time integration steps. In particular, we are looking for the zero crossing of the Laplacian of these metrics (i.e. $\Delta f_t = 0$), however if this criterion is not met then the chosen total integration time is that which maximises F. Since for each metric an integration time $T_f = (T_\sigma, T_{CNR}, T_{SSIM})$ is identified, the optimal stopping instant T is given by the mean value of the T_f instants found, hence $T = (T_\sigma + T_{CNR} + T_{SSIM})/3$. We note that the value of optimal T will vary with the value of β, hence we write $T = T(\beta)$.

In the second stage, we are interested in removing the most amount of noise possible, without compromising image edges. Once the maximum of CNR, S/MSE and PSNR improvement is reached then the sharpness of the edges starts degrading due to edge blurring. Hence, given that for a range of β its respective optimal $T(\beta)$ is known (from the first stage), we aim to find β which maximizes the CNR, S/MSE and $PSNR$ improvement (defined as $f_{imp} = |f_{t+1} - f_t|$, [31]), as well as minimizes the image noise σ. Optimal β is therefore the mean value of the four β obtained for each metric, hence $\beta = (\beta_{CNR} + \beta_{S/MSE} + \beta_{PSNR} + \beta_\sigma)/4$.

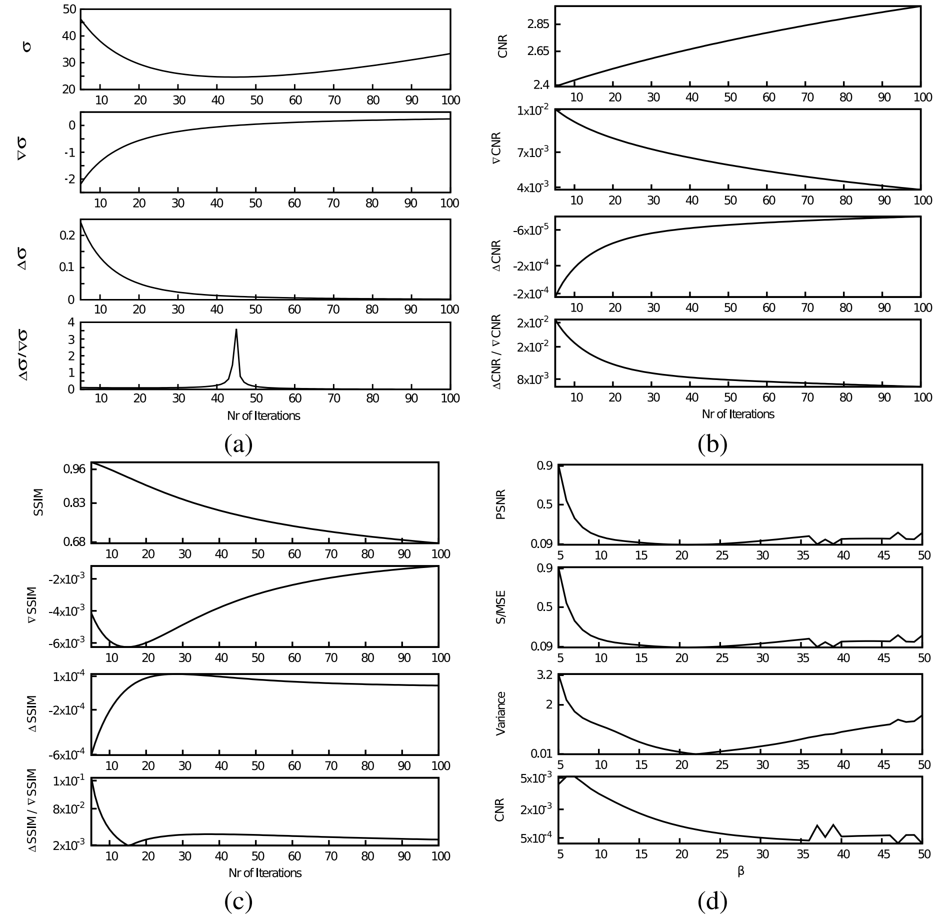

Figure 5: Image quality metrics for dataset 5, as the filtering progresses. The selection of optimal T is found by observing (a)-(c), hence the behaviour of each metric used for the automatic selection of parameters as the number of iterations varies. The selection of optimal β is found by observing (d), hence the variation of each metric improvement. Here we identify the optimal values to be $T = 21$ and $\beta = 27$.

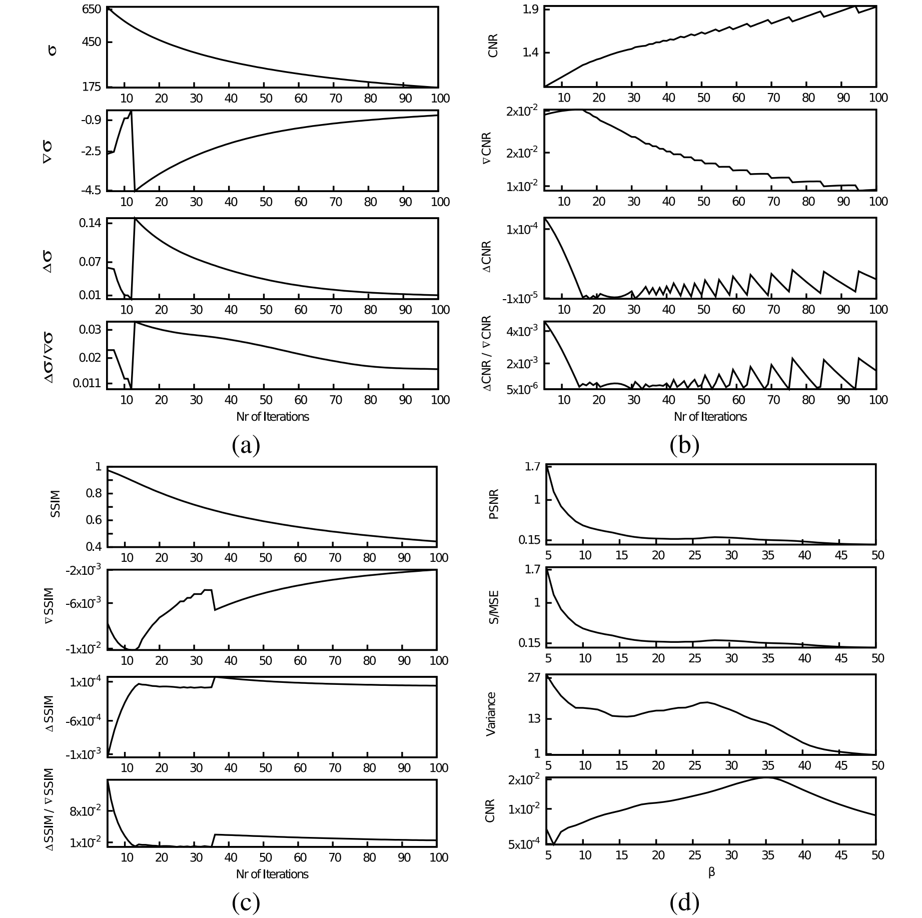

Figure 6: Image quality metrics for dataset 6, as the filtering progresses. The selection of optimal T is found by observing (a)-(c), hence the behaviour of each metric used for the automatic selection of parameters as the number of iterations varies. The selection of optimal β is found by observing (d), hence the variation of each metric improvement. Here we identify the optimal values to be $T = 13$ and $\beta = 32$.

The proposed algorithm is procedurally set out as follows:

Proposed Algorithm:

Step 1. Find the optimal $T(\beta)$, for a range of β:
for $\beta = \beta_{\min} : \beta_{\max}$
  for $t = 0 : \max(t)$
    if Δf_t changes sign
      $T_f = t$;
    else
      $T_f = t$ which maximizes F_f, for $f \in \{\sigma; CNR; SSIM\}$
    endif
  end
end
Optimal $T(\beta)$ subset is then given by $T(\beta) = (T_\sigma + T_{CNR} + T_{SSIM})/3$

Step 2. Find the optimal β from the $T(\beta)$ subset, such that:
for $\beta = \beta_{\min} : \beta_{\max}$
    β_f maximizes f_β, for $f_\beta \in \{CNR_{imp}; S/MSE_{imp}; PSNR_{imp}\}$
      and
    β_f minimizes σ_{imp}
end
Optimal $\beta = (\beta_{CNR} + \beta_{S/MSE} + \beta_{PSNR} + \beta_\sigma)/4$

We now look in detail at the procedure of both stages, taking as examples image datasets 5 and 6, and presenting the results in Figures 5 and 6. It is evident that the values and behaviour of the computed image quality metrics vary considerably between both datasets and hinders direct comparison of absolute values between image datasets. However, on observing the rates of change of the metrics, hence the discrete gradient (Eq. 9), discrete Laplacian (Eq. 10) and the ratio of these (Eq. 11), similar response to the anisotropic diffusion progression can be identified. As expected, either Δf changes sign at some instant t, as seen for $f = SSIM$, or $f = CNR$, in dataset 6 (Figure 6), or the maximum of F marks the beginning of the excessive image degradation for $f = \sigma$. These trends are seen consistently for the metrics used, hence $f \in \{\sigma; CNR; SSIM\}$.

One should note that image metrics are simplistic, since they are each a single number to describe potentially complex images. Indeed, we can see from Figures 5 and 6 that some metrics do not always reach an extremum for a given sweep test or β or T, in which case no parameter choice can be made based on this metric, and it is discarded from the set locally. The use of a varied set of image metrics is therefore important to ensure robustness and quality of the image filtering, and this is in contrast to existing methods for parameter choice. One may also consider the use of additional image metrics, which may improve the robustness and the quality of the image filtering. One could also consider performing the analysis on sub-regions within each image, allowing for a spatially localised quantification, enabling greater sensitivity in the parameter choice of the filtering process.

While this exhaustive parameter search can be computationally intensive, it is evident that one need only evaluate a suitable range of β and T, hence reducing the time required for analysing a given image dataset. The parameter search within a suitable range remains feasible for a stack of 2D images if considered separately. For a 3D volumetric dataset the computational cost is prohibitive and the approach adopted involves identifying parameters from the analysis of individual 2D images within a dataset, and using these directly for the volumetric dataset. This approach appears effective from the numerical tests performed.

6. Numerical Experiments

In this section, we present some examples to show the effectiveness of the proposed approach to perform anisotropic diffusion with automatic parameter selection for β and T. Results have been analysed both in 2D and 3D domain.

6.1. Synthetic Results

Controlled test cases using synthetic images allow us to construct both corrupted and noise-free images. Some results on the progression of the diffusion for both a smooth trigonometric function and a set of step functions, were presented in previous sections and can be seen in Figure 2.

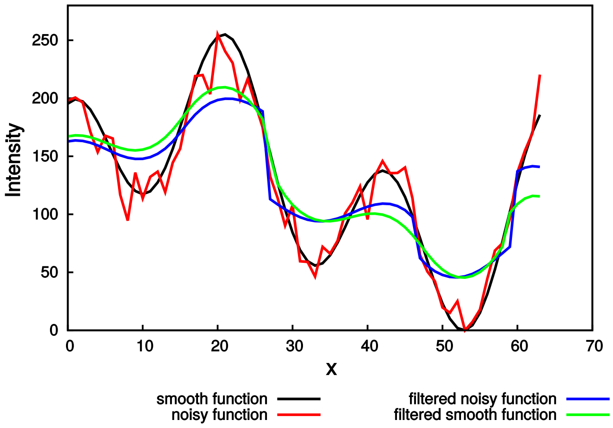

	smooth function	*noisy function*	*filtered function*
CNR	1.7	1.5	2.4
σ	412.6	537.6	188.8
SSIM	0.79	1	0.59
PSNR	42.4	-	37.3

$\beta_{opt} = 19$ $\quad T_{opt} = 544$

Figure 7: Solution of the anisotropic diffusion for dataset 1 (trigonometric function $f(x) = sin(x) + cos(3x)$) corrupted with 10% Gaussian noise. The parameter values $\beta = 19$ and $T = 544$ are identified as optimal using the proposed automatic selection criteria. Image quality metrics are presented in the table.

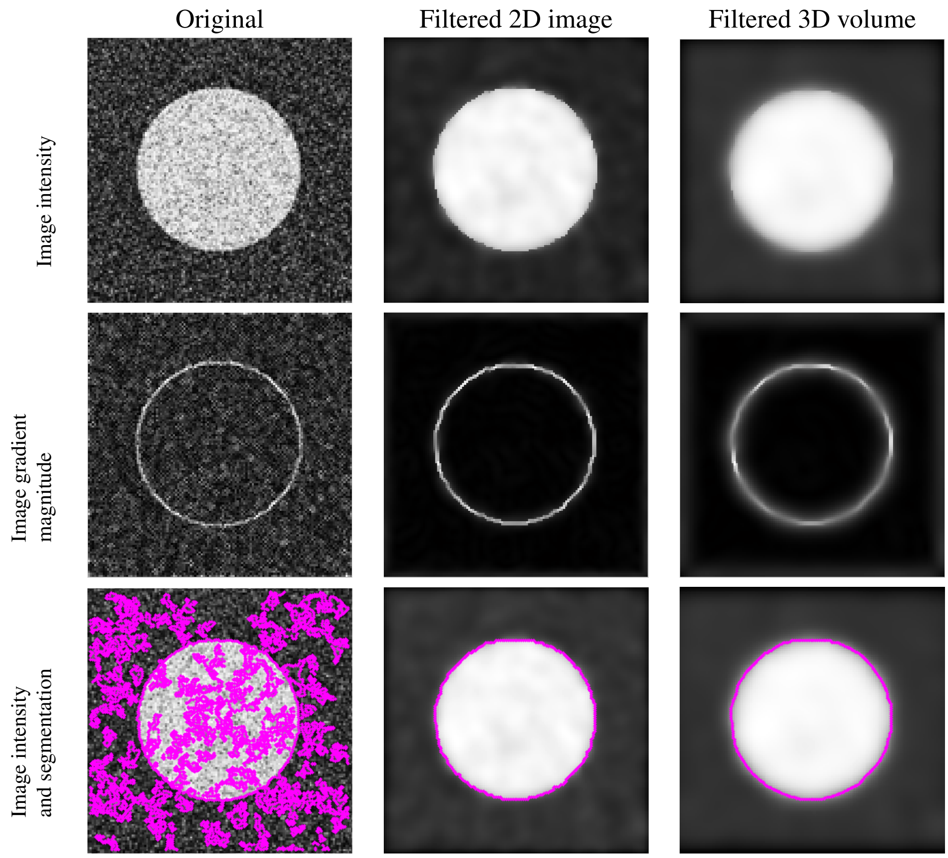

	noisy circle	*filtered in 2D*	*filtered in 3D*
CNR	4.1	6.8	7.5
σ	1169.1	165.1	69.9
SSIM	1	0.16	0.12
PSNR	-	17.9	17.1

Figure 8: Results of filtering using the Perona-Malik method, for a synthetic image of a binary circle with additive Gaussian noise. The filtering is performed on the single 2D image, as well as for the volumetric dataset (analogous to a cylinder). The parameters values $\beta = 35$ and $T = 76$ are identified as optimal using the proposed automatic selection criteria. Image quality metrics are presented in the table.

Here we focus on the effects of noise corruption on the function, and the use of the automatic methods for parameter selection. Our first example is the smooth trigonometric function (dataset 2), with the addition of 10% Gaussian noise, and results of the filtering are shown in Figure 7. When optimal values for β and T are used, based on the image quality metrics, the Perona-Malik method is able to differentiate local and global features and remove noise while maintaining feature objects. From the tabulated image quality metrics presented in Figure 7, we see the expected slight increase on the CNR after filtering, and a significant decrease in the local variance (σ), as the amount of noise is reduced and the filtered function flattens.

Similar findings emerge from the results of the synthetic two dimensional image of the circle (dataset 3) with 10% Gaussian noise, and its extrusion to a 3D cylinder, shown in Figure 8. Both visual and quantitative results show considerable improvements when filtering a stack of images in three dimensions as compared to in two dimensions, which can be easily seen by the improved segmentation obtained.

It should be noted that the Perona-Malik method relies on a Cartesian discretisation for approximating the spatial derivatives of the anisotropic diffusion equation, and as evident from Figure 8, the edge definition deteriorates when it is not aligned to the axes. Alternative discretisations for approximating the spatial derivatives could provide superior results in this regard [10].

6.2. Medical Imaging Results

We focus our attention on the clinically acquired medical data datasets. The results follow those presented earlier in Figure 3, where for incorrect values of β selected, either noise is not removed efficiently ($\beta \ll \beta_{opt}$) or the blurring occurs and edges are excessively diffused ($\beta \gg \beta_{opt}$). A similar behaviour is seen with the total integration time, hence for small number of iterations the filtering is ineffective ($T \ll T_{opt}$), while for large number of iterations feature objects are also filtered ($T \gg T_{opt}$). Parameters T and β may vary within a stack of images, if the images are considered individually. The reason for this is that features and objects of interest in medical image data can regionally vary in size and image characteristics, making it crucial to tune both parameters β and T for each image.

On inspection of the image quality metrics of the filtered datasets using optimal parameters in the Perona-Malik method, reported in Table 2, we find that similar responses are obtained, though the parameter choices are seen to vary. In practical applications, the image quality metrics are not suitable for direct comparison purposes, due to different information present in the datasets (such as imaging modality, patient specific anatomy and regions of interest). However, as noted above, the rate of change of the image quality metrics during the filtering does provide sufficient insight to analyse the individual datasets and give an indication of what parameter choices yield favourable results.

	Dataset 4			**Dataset 6**		
	original	*filtered in 2D*	*filtered in 3D*	*original*	*filtered in 2D*	*filtered in 3D*
CNR	2.3	2.5	2.5	1.9	2.0	2.2
σ	60.2	26.3	11.9	796.0	634.2	617.6
SSIM	1	0.85	0.69	1	0.78	0.62
PSNR	-	34.9	29.0	-	26.0	21.4
	Dataset 8			**Dataset 9**		
	original	*filtered in 2D*	*filtered in 3D*	*original*	*filtered in 2D*	*filtered in 3D*
CNR	41.2	39.9	39.2	59.6	67.7	65.0
σ	880.7	775.8	705.6	191.2	170.8	151.9
SSIM	1	0.94	0.88	1	0.81	0.74
PSNR	-	33.6	28.9	-	22.8	22.3

Table 2: Image quality metrics of the solution of anisotropic diffusion for example datasets.

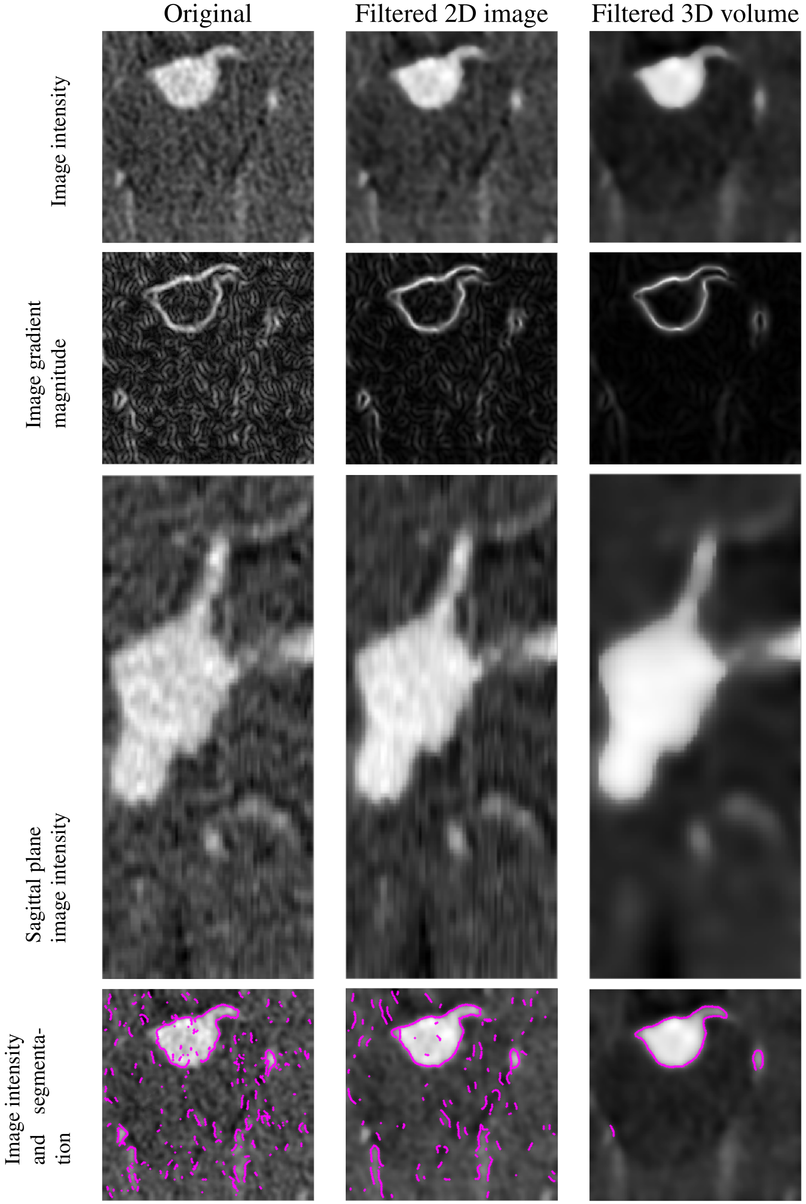

Figure 9: Original and filtered image from dataset 4, with optimal $\beta = 27;\ T = 21$

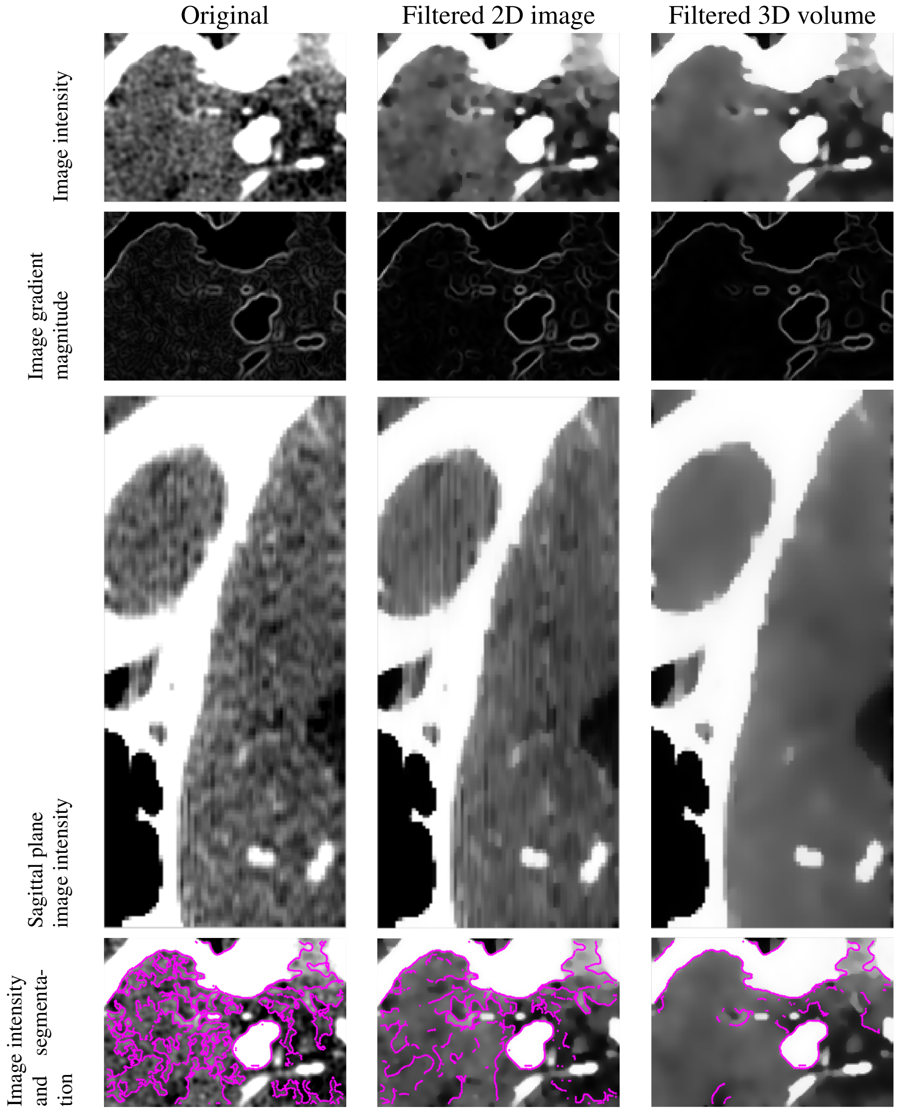

Figure 10: Original and filtered image from dataset 6, with optimal $\beta = 32;\ T = 13$

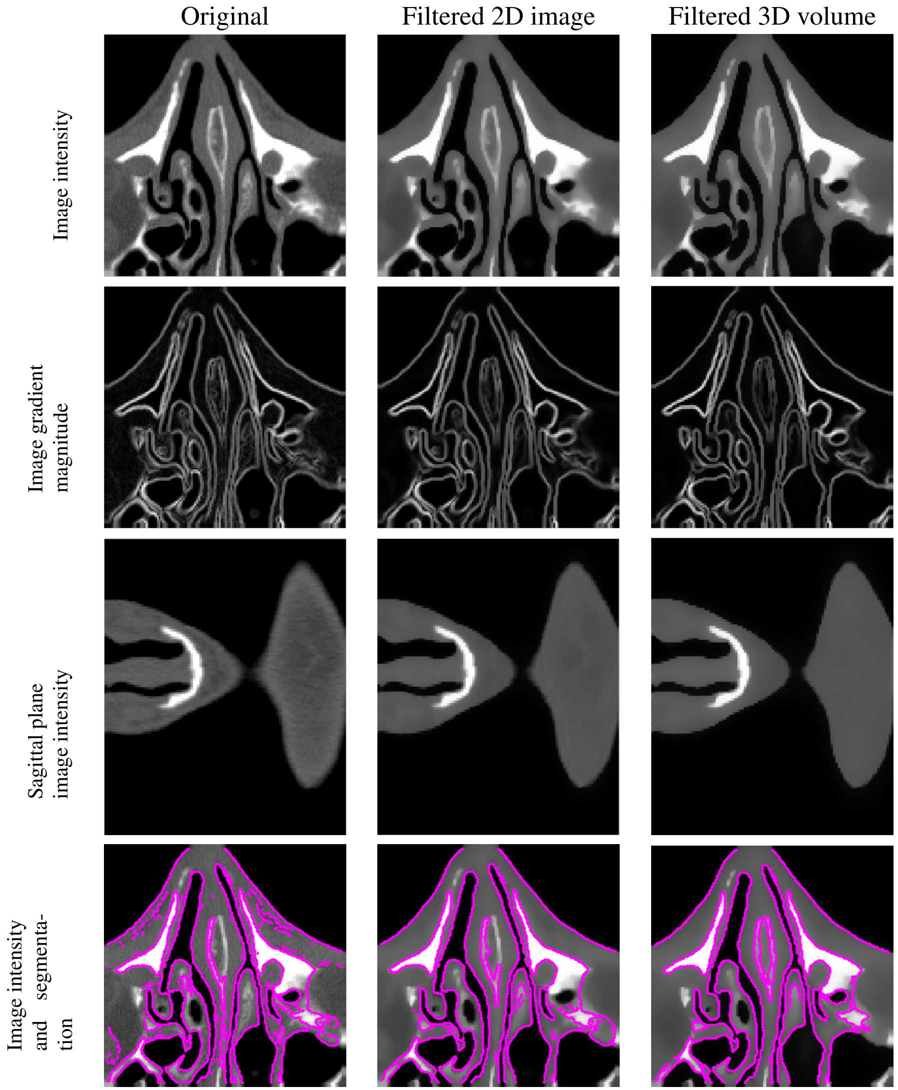

Figure 11: Original and filtered image from dataset 8, with optimal $\beta = 15;\ T = 27$

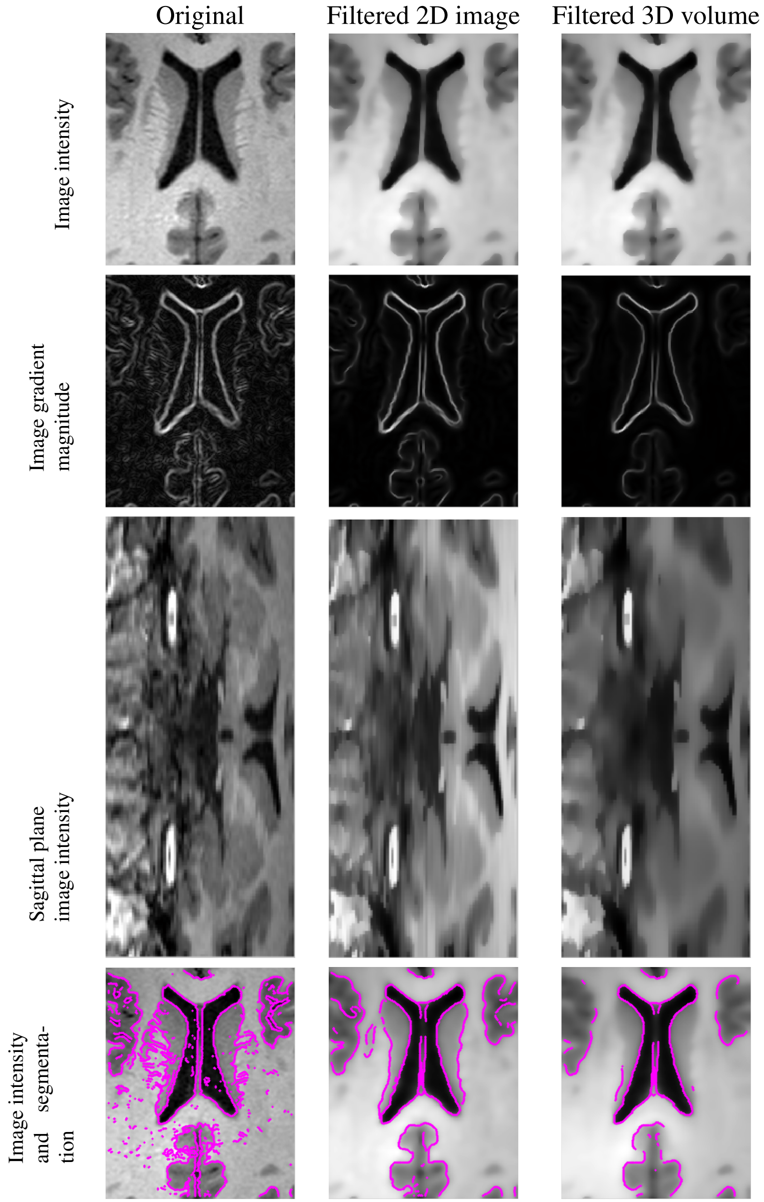

Figure 12: Original and filtered image from dataset 9, with optimal $\beta = 12;\ T = 64$

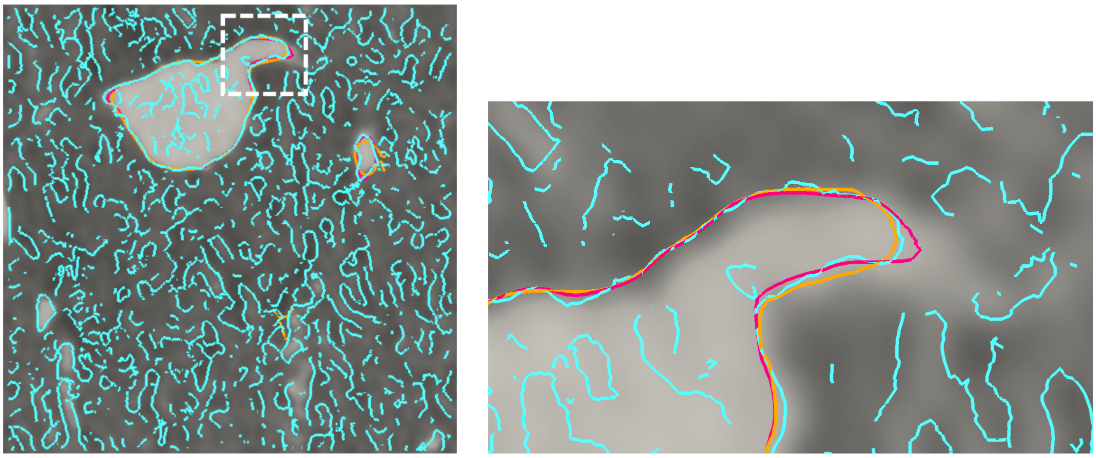

Figure 13: Image dataset 4: contours of lumen boundary of region of interest (left) and detail (right). Segmentation of the image results in: light blue - original geometry; orange - filtered considering single 2D image; magenta - filtered considering volumetric 3D dataset.

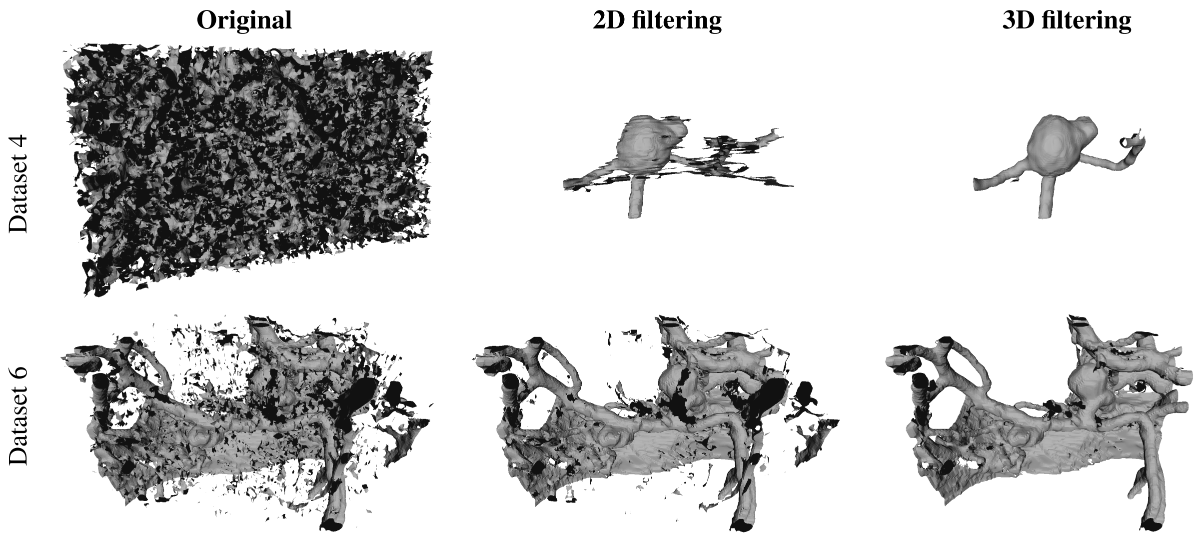

Figure 14: Surface segmentation, applied directly to the 3D volumetric dataset, based on the zero-crossing of the second directional derivative. The reconstructed surface for the original dataset is of poor quality. The reconstructed surfaces for images filtered individually within the stack, show substantial improvement though inter-stack noise is still present to some degree. As the image datasets are filtered in 3D, noise is more effectively identified and removed using information within the stack, resulting in quality reconstructed surfaces of the anatomy. For all these segmentations, in order to allow for clear visibility of the anatomy, all surrounding structures and features have been removed if $|\nabla I| < 20$ for dataset 4 and $|\nabla I| < 40$ for dataset 6 in the marching cubes method for surface extraction.

Results of the filtering process for a selection of the medical image datasets analysed are shown in Figures 9-12, from which it is possible to visually appreciate the quality of the noise removal. From these results it is apparent that the filtering using the 3D volumetric dataset yields superior results compared to those obtained for individual 2D images in a stack. The reason for this is that noise is more effectively identified using information within the stack, as such also more effectively removed while preserving major foreground objects. The exception to this is for image dataset 9, where possibly important features, such as the different cerebral tissue identification, are degraded while dominant features such as the delineation of the ventricles are more clearly identifiable. The reason for this is that the image quality metrics give greater weight to dominant changes in the image as feature objects, and the resulting methodology hence focuses on these.

Additional evaluation of the filtering process is prudent beyond the visual inspection, and we turn our attention to image segmentation. Here, we use an automatic method, in line with the desire to provide an entirely automatic pipeline for processing medical image data. As introduced earlier in Section 3, the zero-crossing of the second directional derivatives of the image intensity is used, both for the individual images as well as for the volumetric data. For ease of visualisation, in the figures only the segmented lines with $|\nabla I| > 10$ are shown. We first compare the segmentation of a section of a cerebral aneurysm, belonging to dataset 4, which can be considered as a representative result and is shown in Figure 13. The result of the filtering is effective in removing much of the noise present, and subsequently also the spurious objects identified in the segmentation of the unprocessed image. The comparison between the filtering performed on the 2D image and the volumetric 3D dataset are similar, though subtly different, with the greatest discrepancy in a region where the vessel is angled with respect to the plane of the image. In this case the information from the volumetric dataset serves to handle the partial volume effects more accurately, since depth information is now available.

From the results of the surface segmentation for image datasets 4 and 6, shown in Figure 14, noticeably superior results are obtained if the filtering is performed on a volumetric dataset as opposed to the individual images in a stack. When the filtering is performed on the volumetric dataset, we observe both that vessels angled with respect to the image plane are processed satisfactorily, and noise across the image stack is more easily identified and removed.

Image quality metrics for the filtered image results are presented in Table 2, where the measures are computed by comparison to the original noisy image. This is done for all image comparison metrics, since, when dealing with medical data, an optimal image is not known. We see that PSNR always decreases for all datasets tested, which is expected and desirable. For datasets acquired using CTA, results show a mean reduction of 38% of image noise (σ) when filtered in 2D (56% and 20% for dataset 4 and 6, respectively), while when 3D filtering is applied, a mean decrease of 51% is seen (80% and 22% for dataset 4 and 6, respectively). This results in a smoother surface segmentation of the anatomical geometry, seen after geometry reconstruction (Figure 14). For the other two modalities (CT and MRI), dataset 8 and 9 (Figures 11 and 12) the same behaviour is seen in Table 2.

The results presented indicate that the proposed automatic method for choosing coefficients for image filtering with the Perona-Malik method, is able to filter noise, preserve important features and enhance the image contrast. For all image modalities, the SSIM is kept high (SSIM $\geq$ 0.62), as well as typically an increase in CNR values after filtering. All the results indicate considerably better performance in segmentation and noise removal when the filtering is applied to the three-dimensional dataset directly.

The results obtained for the medical images were validated by a clinical expert. Such methodology has been adopted in other recent works by the authors, involving numerical simulations of haemodynamics in cerebral arteries [14].

7. Conclusions

The anisotropic diffusion method as proposed by Perona and Malik [30] is widely used in filtering images. The two parameters in the model, namely the gradient threshold constant β (that appears in the diffusion coefficient), and the total diffusion time T (or number of iterations), need to be set *a priori*. In this work we have proposed an automatic method to select coefficients that yield appealing results for both noise suppression and quality object segmentation. The approach is based on *a posteriori* analysis, where the parameter search is reduced by firstly identifying appealing total diffusion times as a function of the gradient threshold constant, hence $T = T(\beta)$, and subsequently choosing a gradient threshold constant from the subset of solutions.

The evaluation of the filtering process, used in order to select the two parameters in the model, rely on image quality metrics. These compare the filtered images to the original noise-corrupted image. The rates of change of the image quality metrics are used to interpret the effects of the diffusion as it progresses, and subsequently a means of identifying the suitable parameters β and T. By taking into consideration a range of image quality metrics, different properties of the image could be tracked during the filtering evolution. While image metrics are simplistic, since they are each a single number to describe potentially complex images, by using a set of metrics we ensure robustness and quality of the image filtering. The additional use of other image metrics may improve the robustness and the quality of the image processing. One could also consider performing the analysis on sub-regions within each image, allowing for a spatially localised quantification, enabling greater sensitivity in the parameter choice of the filtering process.

The automatic filtering method proposed was tested for a set of medical image datasets and synthetic functions. The scope of the approach can be extended for different applications, and may be easily further developed by considering additional quality metrics. The analysis in Section 6 showed that the proposed approach provides a robust solution for the stopping time and gradient threshold, with very promising results. The results obtained for the medical images were validated by a clinical expert. The rates of change of image quality measures are seen to be effective in revealing the response of the anisotropic diffusion to the image datasets.

Although slightly more complex to compute, the filtering process performed in 3D yields more favourable results than considering individually each image of the stack. This is crucial when filtering medical images due to the existent inter-slice noise which can be more efficiently identified and removed by considering the 3D volumetric data.

Acknowledgements

The work has been partially supported by FCT - Fundação para a Ciência e a Tecnologia, through the project EXCL/MAT-NAN/0114/2012 of CEMAT - Center for Computational and Stochastic Mathematics, Instituto Superior Técnico of the University of Lisbon. The medical image datasets are gratefully acknowledged from the following institutions: the Faculty of Medicine of the University of Lisbon and Hospital Santa Maria under the group of Prof. Jorge Campos, and Centro Hospitalar e Universitário de Coimbra.

Appendix A. Anisotropic diffusion

$$\frac{\partial I}{\partial t} = \nabla \cdot (c(|\nabla I|)\,\nabla I) = (c(|\nabla I|)\Delta I + \frac{(c'(|\nabla I|)}{|\nabla I|}\nabla^2 I(\nabla I, \nabla I) \tag{A.1}$$

By setting

$\partial_{\tau\tau} I = (I_{xx} I_y^2 - 2 I_{xy} I_x I_y + I_{yy} I_x^2)/|\nabla I|^2$, as the linear diffusion term in the orthogonal direction of ∇I, and

$\partial_{\eta\eta} I = (I_{xx} I_x^2 - 2 I_{xy} I_x I_y + I_{yy} I_y^2)/|\nabla I|^2$, as the diffusion term in the direction of $|\nabla I|$, the anisotropic equation (Eq. A.1) can be re-written as

$$\nabla \cdot (c(|\nabla I|)\,\nabla I) = c(|\nabla I|)\,\partial_{\tau\tau} I + C'(\nabla I)\partial_{\eta\eta} I, \tag{A.2}$$

with $C(|\nabla I|) = |\nabla I| c(|\nabla I|)$.

Appendix B. Discrete formulation of the Anisotropic diffusion in 2D and 3D

The 2-D discretization procedure is simple and extension of the 1D implementation:

$$\begin{aligned}
\frac{\partial I}{\partial t} &= \nabla \cdot (c \nabla I) \\
&= \frac{\partial}{\partial x}(c\,\frac{\partial I(x,y,t)}{\partial x}) + \frac{\partial}{\partial y}(c\,\frac{\partial I(x,y,t)}{\partial y}) \\
&= \frac{1}{\Delta x^2}\Big(c(x + \frac{\Delta x}{2}, y, t)\,(I(x+\Delta x, y) - I(x,y)) - c(x - \frac{\Delta x}{2}, y, t)\,(I(x,y) - I(x - \Delta x, y)\Big) \\
&+ \frac{1}{\Delta y^2}\Big(c(x, y + \frac{\Delta x}{2}, t)\,(I(x, y + \Delta y) - I(x,y)) - c(x, y - \frac{\Delta y}{2}, t)\,(I(x,y) - I(x, y - \Delta y)\Big) \\
&= \phi_{east} - \phi_{west} + \phi_{north} - \phi_{south}
\end{aligned} \tag{B.1}$$

In the first step of the process, the signal ϕ is computed between neighbouring pixels, while the second step the pixel intensities are updated by the localised sum of pixel contributions:

$$I(t + \Delta t) \simeq \; I(t) + \Delta t\,\frac{\partial I}{\partial t} = I(t) \;+\; \Delta t\,(\phi_{east} - \phi_{west} + \phi_{north} - \phi_{south}) \tag{B.2}$$

The 3D formulation $I(\mathbf{x}) = I(x, y, z)$ follows directly the original anisotropic diffusion in 2D and 1D. The total contribution of each neighbour pixel is now taken from the 26 neighbouring voxels within a $3 \times 3 \times 3$ window. For a d-dimensional problem the stability of this explicit scheme is given by $\Delta t < 1/(2d)$ [40].

References

[1] Atlas, A., Karami, F., Meskine, D., 2014. The peronamalik inequality and application to image denoising. Nonlinear Analysis: Real World Applications 18, 57–68.

[2] Behrenbruch, C.P., Petroudi, S., Bond, S., J., J.D.F., Leong, J. M., B., 2004. Image filtering techniques for medical image post-processing: an overview. The British Journal of Radiology 77, S126–S132.

[3] Bernardes, R., Maduro, C., Serranho, P., Araújo, A., Barbeiro, S., Cunha-Vaz, J., 2010. Improved adaptive complex diffusion despeckling filter. Opt. Express 18, 24048–24059.

[4] Bhadauria, H., Dewal, M., 2013. Medical image denoising using adaptive fusion of curvelet transform and total variation. Computers and Electrical Engineering 39, 1451–1460.

[5] Black, M.J., 1998. Robust anisotropic diffusion. IEEE Transactions on Image Processing 3, 421–432.

[6] Canny, J., 1986. A computational approach to edge detection. IEEE Transactions on Pattern Anal. Machine Intell. PAMI-8, 679–698.

[7] Capuzzo Dolcetta, I., Ferretti, R., 2001. Optimal stopping time formulation of adaptive image filtering. Applied Mathematics and Optimization 43, 245–258.

[8] Chen, Y., Zhang, J., Macione, J., 2009. An improved level set method for brain {MR} images segmentation and bias correction. Computerized Medical Imaging and Graphics 33, 510–519.

[9] Dez, S., Sanchez, S., 2015. Algorithms for contrast enhancement of electronic portal images. Radiation Physics and Chemistry 116, 14–20.

[10] Gambaruto, A., 2015. Processing the image gradient field using a topographic primal sketch approach. International Journal for Numerical Methods in Biomedical Engineering 31.

[11] Gambaruto, A., Peiró, J., Doorly, D., Radaelli, A., 2008. Reconstruction of shape and its effect on flow in arterial conduits. International journal for numerical methods in fluids 57, 495–517.

[12] Gilboa, G., Sochen, N., Zeevi, Y., 2004. Image enhancement and denoising by complex diffusion processes. Pattern Analysis and Machine Intelligence, IEEE Transactions on 26, 1020–1036.

[13] Gilboa, G., Sochen, N., Zeevi, Y., 2006. Estimation of optimal pde-based denoising in the snr sense. Image Processing, IEEE Transactions on 15, 2269–2280.

[14] Goodarzi-Ardakani, V., Tu, X., Gambaruto, A., Velho, I., Tiago, J., Sequeira, A., Pereira, R., 2019. Near-wall flow in cerebral aneurysms. Fluids .

[15] Grewenig, S., Weickert, J., Bruhn, A., 2010. From box filtering to fast explicit diffusion, in: Joint Pattern Recognition Symposium, Springer. pp. 533–542.

[16] Guidotti, P., 2009. A new nonlocal nonlinear diffusion of image processing. Journal of Differential Equations 246, 4731–4742.

[17] Guidotti, P., 2012. A backwardforward regularization of the peronamalik equation. Journal of Differential Equations 252, 3226–3244.

[18] Haralick, R., Watson, L., Laffey, T., 1983. The topographic primal sketch. The International Journal of Robotics Research 2, 50–72.

[19] Hassanpour, H., Samadiani, N., Salehi, S., 2015. Using morphological transforms to enhance the contrast of medical images. The Egyptian Journal of Radiology and Nuclear Medicine 46, 481–489.

[20] Hor, R., Burdin, V., Remy-Neris, O., 2011. Robust local estimation in anisotropic diffusion process, in: Engineering in Medicine and Biology Society, EMBC, 2011 Annual International Conference of the IEEE, pp. 5710–5713.

[21] Ilyevsky, A., Turkel, E., 2010. Stopping criteria for anisotropic pdes in image processing. Journal of Scientific Computing 45, 333–347.

[22] Jain, S., Jagtap, V., Pise, N., 2015. Computer aided melanoma skin cancer detection using image processing. Procedia Computer Science 48, 735 – 740.

[23] Khan, M.A., Khan, T.M., Kittaneh, O., Kong, Y., 2016a. Stopping criterion for anisotropic image diffusion. Optik-International Journal for Light and Electron Optics 127, 156–160.

[24] Khan, T.M., Khan, M.A., Kong, Y., Kittaneh, O., 2016b. Stopping criterion for linear anisotropic image diffusion: a fingerprint image enhancement case. EURASIP Journal on Image and Video Processing 2016, 6.

[25] Khanian, M., Feizi, A., Davari, A., 2014. An optimal pdes-based denoising in medical image processing. Journal of Medical Signals and Sensors 4, 72–83.

[26] Li, X., Chen, T., 1994. Nonlinear diffusion with multiple edginess thresholds. Pattern Recognition 27, 1029–1037.

[27] Marr, D., Hildreth, E., 1980. Theory of edge detection. Proceedings of the Royal Society of London B: Biological Sciences 207, 187–217.

[28] Monteil, J., Beghdadi, A., 1999. A new interpretation and improvement of the nonlinear anisotropic diffusion for image enhancement. IEEE Trans. Pattern Anal. Mach. Intell. 21, 940–946.

[29] Mrázek, P., Navara, M., 2003. Selection of Optimal Stopping Time for Nonlinear Diffusion Filtering. International Journal of Computer Vision 52, 189–203.

[30] Perona, P., Malik, J., 1990. Scale-space and edge detection using anisotropic diffusion. IEEE Transactions on Image Processing 12, 629–639.

[31] Salinas, H., Fernandez, D., 2007. Comparison of pde-based nonlinear diffusion approaches for image enhancement and denoising in optical coherence tomography. Medical Imaging, IEEE Transactions on 26, 761–771.

[32] Shan, X., Sun, J., Guo, Z., 2019. Multiplicative noise removal based on the smooth diffusion equation. Journal of Mathematical Imaging and Vision , 1–17.

[33] Sporring, J., Weickert, J., 1999. Information measures in scale-spaces. Information Theory, IEEE Transactions on 45, 1051–1058.

[34] Tiago, J., Gambaruto, A., Sequeira, A., 2014. Patient-specific blood flow simulations: Setting dirichlet boundary conditions for minimal error with respect to measured data. Mathematical Modelling of Natural Phenomena 9, 98–116.

[35] Tsiotsios, C., M.Petrou, 2013. On the choice of the parameters for anisotropic diffusion in image processing. Pattern Recognition 46, 1369–1381.

[36] Voci, F., Eiho, S., Sugimoto, N., H.Sekibuch, 2004. Estimating the gradient in the Perona-Malik equation. Signal Processing Magazine, IEEE 21, 39–65.

[37] Wang, Z., Bovik, A.C., Sheikh, H.R., Simoncelli, E.P., 2004. Image quality assessment: from error visibility to structural similarity. IEEE Transactions on Image Processing 13, 600–612.

[38] Weickert, J., 1996. Anisotropic Diffusion in Image Processing. Universität Kaiserslautern.

[39] Weickert, J., Heidelberglaan, E., 1997. A review of nonlinear diffusion filtering.

[40] Weickert, J., Romeny, B.T.H., Viergever, M.A., 1998. Efficient and reliable schemes for nonlinear diffusion filtering. IEEE transactions on image processing 7, 398–410.

[41] Yang, G.Z., Burger, P., Firmin, D.N., Underwood, S., 1996. Structure adaptive anisotropic image filtering. Image and Vision Computing 14, 135–145.
[42] Yang, Y., Zhang, W., Liang, D., Yu, N., 2016. Reversible data hiding in medical images with enhanced contrast in texture area. Digital Signal Processing 52, 13 – 24.
[43] Zeng, W., Lu, X., Tan, X., 2015. A local structural adaptive partial differential equation for image denoising. Multimedia Tools and Applications 3, 743–757.